ORIGINAL ARTICLE

Multipath mitigation in GNSS precise point positioning based on trend-surface analysis and multipath hemispherical map

Ran Lu[1,2] · Wen Chen[1,2,3] · Danan Dong[1,2,3] · Zhiren Wang[2] · Chenglong Zhang[1] · Yu Peng[1,2] · Chao Yu[2]

Abstract
The multipath effect reduces the accuracy of pseudorange and carrier phase observations and significantly affects the convergence of precise point positioning (PPP) in an urban high-obstruction environment. The multipath hemispherical map (MHM) is based on the spatial repeatability of the multipath and is used to mitigate the multipath effect. This method is widely used because it is suitable for real-time dynamic and static situations with multipath invariance. Although the MHM algorithm is simple and easy to implement, it ignores the spatial distribution of multipath inside the sky grid. It is not suitable for use in high-frequency multipath corrections. By fitting the multipath trend inside the sky grid, the MHM based on a trend-surface analysis (T-MHM) alleviates the high-frequency and low-frequency multipath simultaneously, improving the accuracy of the baseline solution in the differential mode. We mainly demonstrate the application of T-MHM in PPP, analyze the unmodeled errors, evaluate the multipath correction effect of T-MHM, discuss the optimal modeling days, and test its sensitivity in the scale of the sky grid. Compared to MHM, the experimental results show that using T-MHM in multipath correction improves the positioning accuracy in the horizontal and vertical directions by 21.6 and 13.6%, respectively, and shortens the convergence time by 24.2 and 7.2%, respectively. The T-MHM method is not sensitive to the grid scale of the sky, thus resulting in high efficiency.

Introduction

The precise point positioning (PPP) technology (Malys and Jensen 1990; Zumberge et al. 1997) is an absolute positioning method that caters to global and regional services. PPP is based on the observations from a single global navigation satellite system (GNSS) receiver, given external precise satellite orbit and clock products, and a set of correction documents. Currently, the PPP technology is widely used in urban areas (Zimmermann et al. 2017; Gill et al. 2017; Zhao et al. 2020). The maximum measurement error in multipath interference, which is caused by a high obstruction in such areas, can reach 1/2 the ranging code chip for pseudorange (150 m for GPS C/A code) and 1/4 wavelength for carrier phase (4.76 cm for GPS L1 carrier phase) (Groves and Jiang 2013). However, it is difficult to parameterize such multipath errors because they cannot be eliminated via differential techniques, thereby affecting the positioning accuracy and convergence time of the PPP.

Multipath mitigation methods can be broadly divided into two categories, i.e., hardware improvement and data processing. The hardware improvement mainly focuses on antenna design and receiver improvement. The existing antenna design technologies include patch elements placed on choke rings (Dinius 1995) and dual-polarization antennas (Groves et al. 2010). There have been several attempts to improve the performance of the receiver, including the use of concepts such as "narrow correlator" delay-locked loop (Dierendonck et al. 1992) and multipath estimating delay-locked loop (Nee et al. 1994; Nee 1995). However, hardware

✉ Wen Chen
wchen@sist.ecnu.edu.cn

1   Key Laboratory of Geographic Information Science, East China Normal University, No. 500 Dongchuan Road, Shanghai 200241, China

2   Engineering Center of SHMEC for Space Information and GNSS, East China Normal University, No. 500 Dongchuan Road, Shanghai 200241, China

3   Shanghai Key Laboratory of Multidimensional Information Processing, East China Normal University, No. 500 Dongchuan Road, Shanghai 200241, China

improvement can only partially eliminate multipath errors, and it also increases the hardware cost.

As to data processing implementation, there are two existing categories of multipath mitigation methods. The first category is a data post-processing method that mainly includes empirical mode decomposition (Dai et al. 2006), wavelet analysis (Zhong et al. 2008; Su et al. 2018), and adaptive finite impulse response filtering (Ge et al. 2000). This category uses various filtering methods to denoise the observations, separate the multipath error time series, and then carry out post-processing correction using the observation series. This method, thus, is not suitable in real-time applications.

The second category is the real-time mitigation method, which maximizes the temporal or spatial repeatability of multipath for real-time multipath mitigation. The sidereal filtering (Genrich and Bock 1992) is a real-time multipath correction method that uses GNSS time-domain repeatability in a static observation environment (Bock et al. 2000; Zhong et al. 2010). If the surrounding observation environment remains unchanged for a fixed station, the multipath effect is related to the geometric relationship between the satellite and the station. Therefore, the multipath values of previous orbital cycles can be used to correct the current GNSS observations. The GPS satellites revisit a static ground station with a period approximately equal to a sidereal day of 23 h 56 min 4 s (86,164 s) (Choi et al. 2004). Researchers have implemented various GPS multipath mitigation studies in the position- and observation-domains (Ragheb et al. 2007) and applied them to the PPP mode. Takasu (2006) used position-domain sidereal filtering to correct the multipath error of GPS precise point positioning. In addition, Hung and Rau (2013) utilized a band-pass filter to improve position-domain multipath error correction efficiency. Also, Atkins and Ziebart (2016) proposed a sidereal filtering algorithm based on observation-domain to alleviate the multipath error in PPP applications. Unlike the position-domain, the observation-domain can take advantage of the fact that the repeat time of each GPS satellite is slightly different, which is more effective for mitigating the high-frequency multipath error. However, the sidereal filtering method requires an accurate satellite revisit time, further increasing the calculation cost in real-time applications. This method is even more complex for GLONASS, Galileo, and BDS multi-system joint positioning. In addition, sidereal filtering is only applicable in the static positioning mode.

Another real-time multipath mitigation approach is to utilize the spatial-domain repeatability of multipath. This one includes the multipath spherical harmonic model (Cohen and Parkinson 1991), multipath stacking (MPS) (Fuhrmann et al. 2015), and the multipath hemispherical map (MHM) (Dong et al. 2016a). The multipath effect of stations in stable environments is only related to the elevation and azimuth angles of the satellite, irrespective of the type of

satellite. These methods do not require the satellite orbital repeat time and are suitable for static and dynamic environments with stable surrounding environments. The multipath spherical harmonic model considered a sky grid resolution of $30° \times 30°$ in the multipath mitigation method based on the spherical harmonic. The positioning accuracy can be increased by reducing the grid size. For example, a resolution of $1° \times 1°$ is equivalent to realizing a spherical harmonic model of $1/360°$ (13,321 spherical harmonic coefficients); however, it requires an extensive calculation and is also challenging to implement. The MPS and MHM methods divide the sky map into $1° \times 1°$ grids according to the equal lattice area and equal lattice sizes, respectively, and consider the average of the residuals of all satellites in each grid as the multipath correction value. It is easier to achieve a resolution of $1° \times 1°$ with these methods. Still, the researchers found that MHM can effectively alleviate low-frequency multipath, but its improvement on high-frequency multipath is not obvious. This is mainly because the spatial trend of the multipath inside the grid is overlooked. To overcome this problem, Zheng et al. (2019) divided the grid more finely in the low elevation angle region (0–60°) according to the frequency distribution of the multipath and empirically divided the MHM into $0.2° \times 0.2° \times 1°$. Thus, this method is only limited to specific situations. Wang et al. (2019) introduced the trend-surface modeling method (T-MHM) to fit the spatial distribution of the multipath within the grid, which is more flexible and ideal for real-time applications. The experimental results demonstrate that the T-MHM method alleviates high- and low-frequency multipath in differential modes (Wang et al. 2020).

We demonstrated the feasibility of the T-MHM method for PPP. First, the data processing method of PPP and the T-MHM model are explained. The experimental environment and data collection process are given, and the optimal modeling days of multipath, residual characteristics before and after multipath correction, and different grid sizes are discussed. Finally, the conclusions and future work are provided.

Methodology

Based on various processing strategies of ionospheric errors, the PPP function models are mainly divided into two categories. They are the ionospheric-free combination model and the undifferenced and uncombined model (Zhang et al. 2013). The ionospheric-free combination model eliminates the adverse impact of the first-order ionospheric delay through a linear combination of observations of two frequencies. It further amplifies the observation noise by a factor of 2 to 3 and reduces the multipath error (Liu et al. 2017). The undifferenced and uncombined PPP model uses external ionospheric

products (GIMs) to eliminate the ionospheric effect. It avoids the amplification of observation noise and the unmodeled multipath error caused by an ionospheric-free combination (Zhou 2020).

Retrieving multipath from PPP model

The following equations apply GPS undifferenced and uncombined dual-frequency pseudorange and carrier phase observations:

$$P_{r, j}^{s} = \rho_{r}^{s} + c(dt_{r} - dt^{s}) + trop_{r}^{s} + ion_{r}^{s}$$
$$+ ucd_{r, j} - ucd_{j}^{s} + MP_{r, j}^{s} + \varepsilon_{r, j}^{s} \tag{1}$$

$$L_{r, j}^{s} = \rho_{r}^{s} + c(dt_{r} - dt^{s}) + trop_{r}^{s} - ion_{r}^{s} + upd_{r, j}$$
$$- upd_{j}^{s} + \lambda_{j} N_{r, j}^{s} + \Delta\Phi_{GPWU} + ML_{r, j}^{s} + \xi_{r, j}^{s} \tag{2}$$

where indices s, r, and j ($j = 1, 2$) are the PRN number, receiver ID, and observation frequency band number, respectively; ρ_{r}^{s} denotes the geometric distance from the satellite to the receiver; dt_{r} and dt^{s} are the receiver and the satellite clock offsets, respectively; $trop_{r}^{s}$ is the tropospheric delay of the propagation path; ion_{r}^{s} is the first-order term of the ionospheric delay of the signal propagation path; $ucd_{r, j}$ and ucd_{j}^{s} are the uncalibrated pseudorange delays of the receiver and satellite, respectively; $upd_{r, j}$ and upd_{j}^{s} are the uncalibrated carrier phase delays of the receiver and satellite, respectively; λ_{i} is the carrier phase wavelength corresponding to frequency j; $N_{r, j}^{s}$ is the carrier phase ambiguity; c is the speed of light; $\Delta\Phi_{GPWU}$ is the ground-based carrier phase wind-up; $MP_{r, j}^{s}$ and $ML_{r, j}^{s}$ are pseudorange and carrier phase multipath errors, respectively; $\varepsilon_{r, j}^{s}$ and $\xi_{r, j}^{s}$ are random noise errors corresponding to pseudorange and carrier phase observations. The units of all variables except ambiguity are meters. Note that when the receiver antenna is rotating, a ground-based carrier phase wind-up term emerges in the carrier phase observation equation, while there is no ground-based carrier phase wind-up in pseudorange observation. The $\Delta\Phi_{GPWU}$ term is coupled with the receiver clock term dt_{r}, so that they can be merged into one "clock" parameter dt_{r}^{L} in carrier phase observation. Such a parameterization is called the "decoupled clock" model (Collins 2008; Banville and Tang 2010; Dong et al. 2016b), which fits both static and kinematic positioning.

All datasets were processed with the GAMP (GNSS analysis software for multi-constellation and multi-frequency precise positioning) software (Zhou et al. 2018). The processing strategies are shown in Table 1. In the table, PCO and PCV represent antenna phase center offset and

variations, respectively. Precision orbit and clock products can be found at http://ftp.aiub.unibe.ch/CODE/. The PCO and PCV of GPS can be obtained at ftp://igs.org/pub/station/general/pcv_archive/.

The receiver positions are estimated as daily solutions using the Kalman filter. By substituting these parameters into (1) and (2), the unprocessed residuals $\eta_{r, j}^{s}$ and $\varphi_{r, j}^{s}$ can be extracted as follows:

$$\eta_{r, j}^{s} = P_{r, j}^{s} - \rho_{r}^{s} - c(dt_{r} - dt^{s}) - trop_{r}^{s} - ion_{r}^{s} - ucd_{r, j} + ucd_{j}^{s} \tag{3}$$

$$\varphi_{r, j}^{s} = L_{r, j}^{s} - \rho_{r}^{s} - c(dt_{r}^{L} - dt^{s}) - trop_{r}^{s}$$
$$+ ion_{r}^{s} - upd_{r, j} + upd_{j}^{s} - \lambda_{j} N_{r, j}^{s} \tag{4}$$

Methodology of T-MHM

Figure 1 shows the T-MHM flowchart, which mainly comprises four steps. First, we calculate the PPP static positioning solutions for the four systems (GPS, GLONASS, Galileo, and BDS) of the station every day for a week (7 days). The mean value of these solutions is substituted into PPP-fixed mode to solve the residuals, azimuths, and elevation angles. Second, the residuals are divided into a sky grid of a specific size based on the azimuth and elevation angles to carry out the trend-surface analysis for the residuals inside the specific grid. Next, we perform statistical tests on the results of the trend-surface analysis. If the model passes the statistical test, the trend-surface fitting coefficients are stored; otherwise, the mean value of residuals within the grid is counted, similar to the MHM. Finally, the correction table, i.e., grid position and correction model coefficients, is generated. To implement the multipath correction, we first query the fitting coefficient of trend-surface from the multipath correction table according to the satellite position information, calculate the multipath model value from (6), (7), (8), and directly remove the multipath model value from the original observation values after that.

When T-MHM is used for trend-surface analysis to fit the spatial variation of multipath residuals inside the grid, the residuals can be expressed as:

$$mp_{i}(az_{i}, el_{i}) = \widehat{mp_{i}}(az_{i}, el_{i}) + Y_{i} \tag{5}$$

where i is the index of the equations inside a particular grid. If there exist t points inside the grid, then $i = 1, 2, ... , t$; mp_{i} is the observed residual, i.e., η and φ in (3), (4); $\widehat{mp_{i}}$ is the estimate of the multipath value; Y_{i} is the unfitted residual within the grid; az_{i} and el_{i} are the azimuth and elevation angles of the satellite, respectively.

Table 1 Data processing strategies

Satellite system	GPS: L1/L2, P1/P2	
Filtering estimation	Kalman filter	
Sampling rate	1 Hz	
Elevation cutoff	10°	
Error model	Satellite orbit	CODE precise orbit (15-min interval)
	Satellite clock	CODE precise clock (5-s interval)
	Tropospheric delay	Zenith wet delay: estimation of random walk process. Process noise:10^{-8} m^2/s (Li and Zhang 2014)
	Ionospheric delay	Parameter process estimation of random walk. Process noise:0.0016 m^2/s (Geng and Bock 2016)
	Stochastic model	Satellite elevation angle weighting
	Antenna phase center	The PCO and PCV of GPS use the data provided by igs14.atx
	Space-based carrier phase wind-up (Wu et al. 1993)	External model correction (Kouba 2015)
	Tidal load	Solid tide, polar tide, and ocean tide corrected using IERS convention 2010
	Relativity effects, Earth rotation	External model correction (Kouba 2015)
Unknown parameters	Receiver position	Estimated as constants for daily solution
	Receiver clock offset	Estimated as white noise
	Ambiguity	Estimated as constant for each arc: float value

The T-MHM uses polynomial function to fit equations, and the commonly used trend-surface fitting equations are given as:

$$\widehat{mp_i}(az_i, el_i) = c_0 + c_1 az_i + c_2 el_i \tag{6}$$

$$\widehat{mp_i}(az_i, el_i) = c_0 + c_1 az_i + c_2 el_i \\ + c_3 az_i el_i + c_4 az_i^2 + c_5 el_i^2 \tag{7}$$

$$\widehat{mp_i}(az_i, el_i) = c_0 + c_1 az_i + c_2 el_i + c_3 az_i el_i + c_4 az_i^2 \\ + c_5 el_i^2 + c_6 az_i^2 el_i + c_7 az_i az_i^2 + c_8 az_i^3 + c_9 el_i^3 \tag{8}$$

Equations (6), (7), (8) represent a linear, quadratic, and cubic trend-surface fitting, respectively. $c_0 - c_9$ are the fitted trend-surface coefficients. The fitting coefficient of the trend surface can be obtained by least square.

To avoid overfitting and underfitting, it is necessary to carry out a goodness of fit and significance test on the fitting coefficient. The corresponding equations are given in Fig. 1. Equations (9)–(14) are regression sum of squares, the total sum of squares, ratio, residual square sum, F-test, and successive significance test. $\overline{mp}$ is the mean of the residuals; z is the total number of observed residuals within the grid; p and q are the degrees of freedom of trend-surface order K and $K + 1$, respectively; F obeys the F-distribution with degree of freedom $(p - 1, z - p)$; $F_{K \to K+1}$ obeys the F-distribution with degree of freedom $(q - p, z - q)$.

Data description

We placed the Trimble BD982 GNSS receiver on the platform on the fourth floor of the information building of East China Normal University. We collected data for days of the year (DOY) 272–279 in 2019 for eight consecutive days. The data sampling rate was 1 Hz, and the satellite elevation angle cutoff was 10°. In Fig. 2, the red circle indicates the position of the receiver, and the buildings in the southeast of the receiver are blocked.

The multipath sky map in Fig. 3 indicates that the multipath error of the experimental environment is the strongest for azimuth angles between 40 and 60° and between 230 and 320°. As shown in Fig. 2, most of the multipath error is due to the reflection of the southeast wall. The probability densities of pseudorange and carrier phase residuals in Fig. 3 are similar to the normal distribution. The pseudorange residuals are basically distributed between −2 and 2 m, and nearly 95% of them are between −1 and 1 m. The carrier phase residuals are distributed between −0.025 and 0.025 m, and most values are between −0.01 and 0.01 m. To minimize the impact of pseudorange multipath on PPP initial solutions, we corrected the pseudorange and carrier phase multipath simultaneously.

Results and discussion

Three indicators are adopted to evaluate the correction effect of the multipath model:
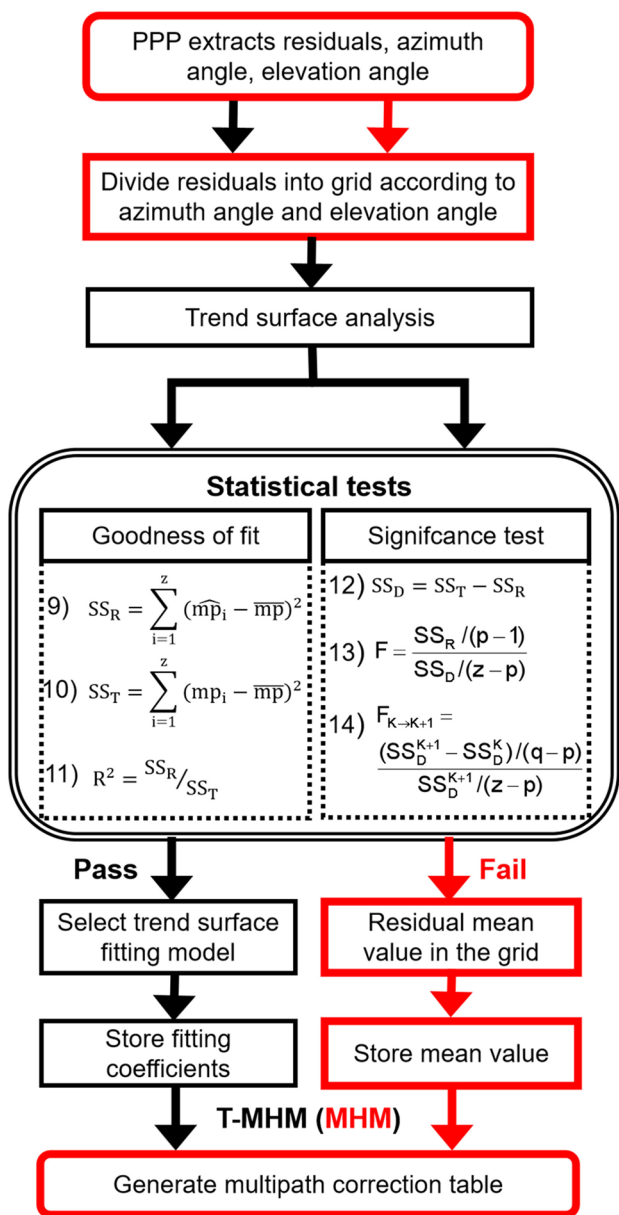
Fig. 1 T-MHM construction flowchart. If T-MHM fails the statistical tests, then it is the same as MHM. The model flow of T-MHM includes MHM. The latter is marked in red

Fig. 2 Environment of experiment. Bottom left is azimuth information

Optimal modeling days of T-MHM

We extracted pseudorange and carrier phase residuals from undifferenced and uncombined PPP solutions for DOY 272–278 and constructed MHM and T-MHM models with a spatial resolution of $1° \times 1°$. Figure 4 shows the positioning error of the corresponding model for the first 5000 epochs. The results of both models are significantly improved compared to the uncorrected case. The T-MHM solutions approach the convergence line, i.e., the black dotted line, earlier than MHM. The statistics in Table 2 indicate that the horizontal and vertical accuracies of T-MHM are 21.6 and 13.6% higher than those of MHM.

Figure 5 delineates the multipath model correction value sequences of satellite PRN 02 from both methods. The right panels are a magnification of epochs 1–5000 and 30,000–40,000. The general trend of these two curves is identical, but the T-MHM model contains more information than MHM. The multipath curve from MHM is similar to that of rectangular waves and lacks high-frequency information. Meanwhile, the T-MHM model can eliminate both high- and low-frequency multipaths because the spatial distribution of multipath in each sky grid is described in detail.

Figure 6 shows the correction rates according to the RMSE in Table 2. It is seen that the correction rates of both methods are relatively stable when modeling with 4–7 days observation data. The advantage of using multi-day data for modeling is that it can increase the sample size and smoothen some unmodeled errors. The smoothing effect is more significant in the T-MHM than MHM because it generates a more detailed multipath model.

Figure 7 shows the histogram of the convergence time for the uncorrected and the two modeling methods over the 7-day modeling span. Due to the correlation between ionospheric delay, phase ambiguity, and multipath, the

Positioning accuracy is measured by the root-mean square error (RMSE) of the positioning errors in East, North, and Vertical directions.

Convergence time refers to the epoch, after which the positioning error remains below 0.1 m for 5 min.

Correction rate of positioning accuracy, convergence time, and residual are calculated using the formula $(1 - r_2/r_1) \times 100\%$, where r_1 and r_2 are the corresponding statistical results of positioning accuracy, convergence time, and residual before and after multipath correction, respectively.

Fig. 3 Multipath sky map and histogram of residuals. Top and bottom panels describe pseudorange observations and carrier phase observations, respectively
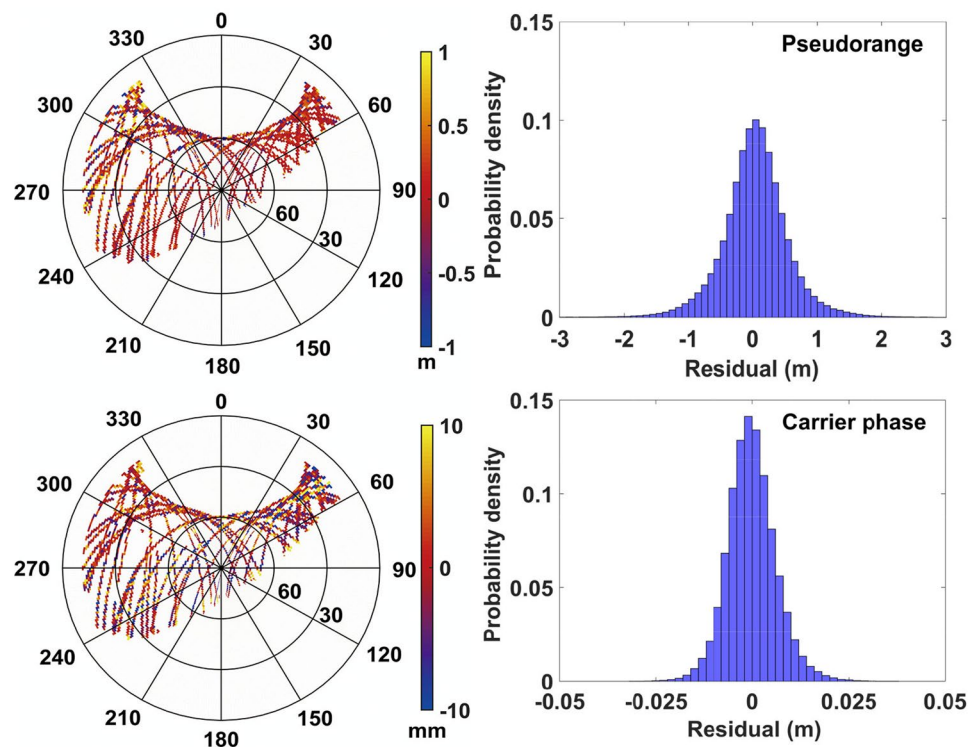
undifferenced and uncombined PPP requires more time to separate the multipath and the other two parameters than that required for the combined PPP, thus increasing the convergence time of PPP solution (Pan et al. 2019). It can be seen from the figure that the convergence speed increases after the correction of multipath, particularly for the T-MHM method. Compared to MHM, the horizontal and vertical convergence time for T-MHM is reduced by 24.2 and 7.2%, respectively.

We also calculate the standard deviation (STD) of the positioning errors from the two methods, based on the modeling for DOY 275–278, i.e., days 4–7. Figure 8 shows the STD values of East, North, and Vertical for T-MHM as 0.0243, 0.0492, and 0.0546 m, respectively. From the above results, it can be inferred that the T-MHM model can correct the multipath accurately by using data observed for four days, and the PPP positioning accuracy can reach the centimeters under a severe obstruction environment.

Residual analysis

We build the MHM and T-MHM models based on the data for four days before DOY 277–279, correct them, and extract the pseudorange and carrier phase residual sequences of satellite PRN 02 before and after multipath correction. Figure 9 shows that the pseudorange and carrier phase residual sequences shifted by adding constants of 2 and 0.02 m, respectively. The figure shows that the DOY 277–279 residual sequence of PPP solution has a strong spatiotemporal correlation. The uncorrected residual sequence shows the effect of high- and low-frequency variation superposition. Although the MHM eliminates the periodic fluctuations in the residual sequence, some high-frequency errors persist. The T-MHM shows the ability to weaken the high-frequency multipath, making the residual sequence smoother, as shown in the highlighted parts with dark boxes. Table 3 shows the STD values of the above residual sequences and the correction rate of residual after multipath mitigation. The average residual correction rate of T-MHM is close to 50.6%, which is 14% higher than that of MHM. Compared to the pseudorange residual correction rate, the carrier phase residual correction rate is increased by 5.5% on average.

We analyze the spectrum of unmodeled errors before and after multipath correction. Figure 10 shows the power spectral density of the carrier phase residuals in Fig. 9. It can be found that the correction effect of T-MHM is better than that of MHM in both high- and low-frequency bands. In the high-frequency band $8 \times 10^{-2} \leq f \leq 5 \times 10^{0}$, the correction in T-MHM is about 3–5 dB less than that in MHM. After applying the T-MHM correction, the power spectral density smoothens. In this case, we can assume that the main unmodeled error in the residual sequence is the observation noise.

In addition, based on the time-domain Allan variance theory (IEEE 2008a, b), we analyze the unmodeled error characteristics before and after multipath correction. There are two types of Allan variance grouping: overlapping and non-overlapping. In this study, overlapping is used as an
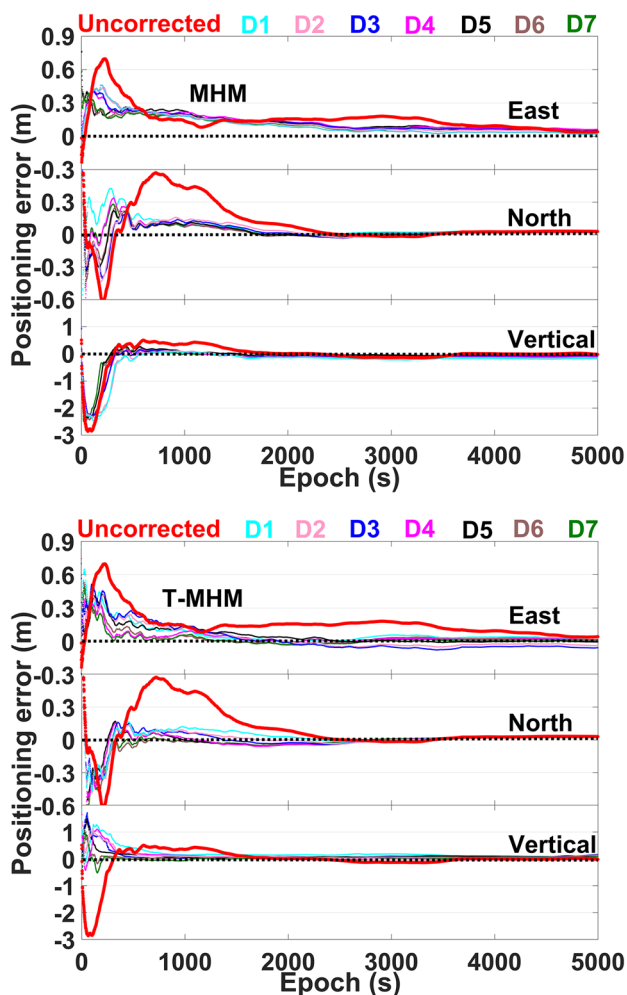
$$Y_i(\tau)_{\tau=e\tau_0} = \frac{1}{e} \sum_{x=i}^{i+e-1} y_i \qquad 1 \leq i \leq N - 2e + 1$$

$$(15)$$

The mathematical form of overlapping Allan variance is defined as follows (Riley 2008)

$$\sigma^2(\tau) = \frac{1}{2(N - 2e + 1)} \sum_{h=1}^{N-2e+1} [Y_{h+e}(\tau) - Y_h(\tau)]^2 \qquad (16)$$

The Allan deviation is:

$$\sigma(\tau) = \sqrt{\sigma^2(\tau)} \qquad (17)$$

where y_i is the data set; the symbol N denotes the sample length and τ_0 is the sampling period divided into h groups; each group contains e sample points. The correlation time of each group is $\tau = e\tau_0$.

There are four typical stochastic processes in GNSS applications: white noise (WN), random walk noise, first-order Gaussian Markov noise (GM), and flicker noise. According to the typical Allan deviation diagrams of different noise types given by IEEE (2008a, b), it can be determined that they have the characteristics of $-1/2$, $+1/2$, $\pm 1/2$, and 0 slopes, respectively. The details are listed in Table 4. First, we need to calculate the variance of the residual sequence according to (16). Then, we calculate the slope of correlation time by the log–log transformation. Finally, according to the curve slope of Allan deviation in Table 4, we can judge the corresponding residual category.

Figure 11 displays the Allan deviation curve of PRN 02 between epochs 6500 and 10,000. The noise intensity of WN can be determined by $\sigma(1)$. The first-order GM noise parameter can be obtained from the Allan curve at the highest point of intersection with the slope of $\pm 1/2$, where the x and y axes represent cluster time and Allan deviation, respectively. The correlation time and noise intensity are calculated by substituting them into Table 4. It is observed that WN and first-order GM are included in the unmodeled errors of pseudorange and carrier phase simultaneously.

In Fig. 11, the first-order GM plays a major role before multipath correction. According to the analysis of Li et al. (2018), the first-order GM plays an important role in the
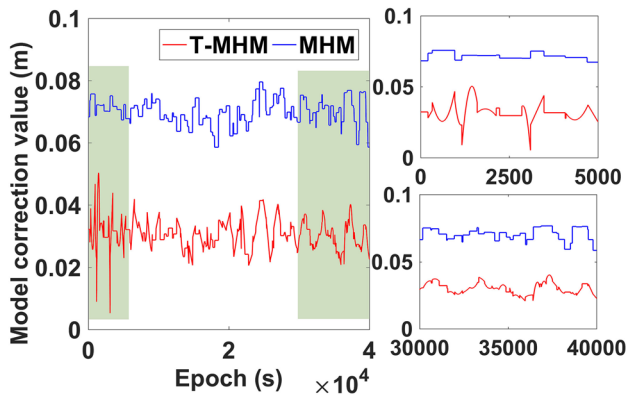
Fig. 4 Positioning errors in East, North, and Vertical for eight strategies with MHM (top) and T-MHM (bottom). The uncorrected results of DOY 279 are labeled "Uncorrected". Based on the number of days of data collection to build the multipath models, i.e., from days 1 to 7, the corrected results of DOY 279 are identified by D1–D7, respectively

analysis tool because it has better stability and better estimation accuracy than the non-overlapping type (Zhang et al. 2015).

The average value of overlapping grouping is:

Table 2 RMSE (m) of MHM and T-MHM in East, North, and Vertical directions

		Uncorrected	D1	D2	D3	D4	D5	D6	D7
East	MHM	0.0682	0.0347	0.0343	0.0362	0.0308	0.0316	0.0311	0.0284
	T-MHM	0.0682	0.0331	0.0312	0.0299	0.0283	0.0296	0.0272	0.0280
North	MHM	0.1093	0.0547	0.0483	0.0596	0.0629	0.0583	0.0606	0.0562
	T-MHM	0.1093	0.0617	0.0496	0.0504	0.0394	0.0406	0.0445	0.0483
Vertical	MHM	0.1545	0.1056	0.1017	0.0859	0.0835	0.0766	0.0819	0.0841
	T-MHM	0.1545	0.0846	0.0887	0.0899	0.0707	0.0728	0.0679	0.0713

Fig. 5 Model correction values of satellite PRN 02 from T-MHM and MHM in DOY 279. The values for T-MHM and MHM are shifted by 0.03 and 0.07 m, respectively
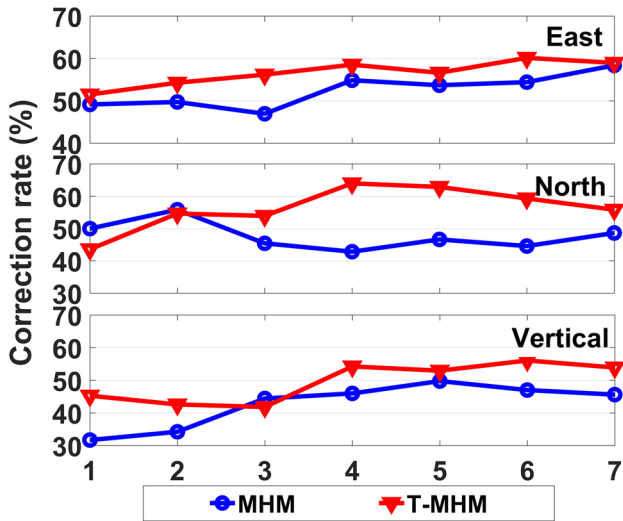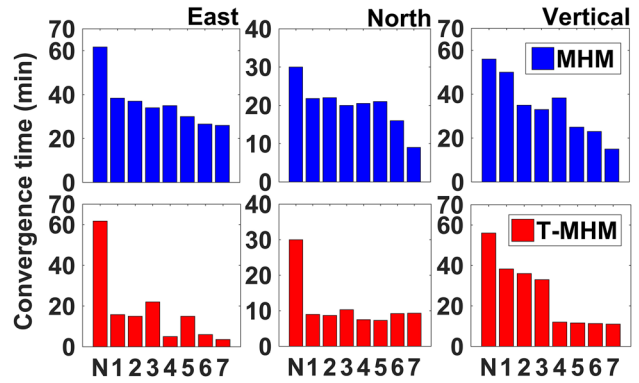

Fig. 7 Convergence time for PPP solutions with uncorrected multipath (N) and modeled multipath with MHM (top) and T-MHM (bottom). The x-axis labels 1–7 indicate the number of days used for the multipath modeling

Fig. 6 RMSE correction rate (%) of seven strategies in East, North, and Vertical directions. The x-axis identifies the number of days used for the modeling

case of strong multipath, while the WN mainly arises from the receiver. After the T-MHM corrects the multipath, the noise intensity of the first-order GM is reduced to a certain extent, but the WN is not improved. Especially in the top panels, the Allan curve of the pseudorange is close to that of WN sequence after T-MHM correction, and the curves for the three days are similar.

Different grid sizes

Considering the optimal modeling days 4–7, we use the DOY 275–278 model to build T-MHM and MHM models with nine different grid sizes and then utilize these models to correct DOY 279. To evaluate the impact of different grid

sizes modeling on the positioning performance, we select the positioning errors sequences of DOY 279 for epochs 1–2000 before PPP convergence, as shown in Fig. 12. In the top panel, the positioning error of PPP solution increases significantly in three directions when the grid size of MHM increases from 1×1 to 2×2. As the grid size increases, the positioning error of MHM before convergence changes greatly, and the stability of the sequence decreases. On the contrary, in the bottom panel, the dispersion of T-MHM positioning error in three directions does not show such a significant change seen for MHM. To quantitatively evaluate the positioning results of MHM and T-MHM for different grid sizes, we calculate the positioning accuracy and convergence time of PPP.

For positioning accuracy, the corresponding RMSE results are calculated. We compare the RMSE results of MHM and T-MHM in the East, North, and Vertical directions in Fig. 13. The positioning accuracy of MHM worsens more seriously relative to T-MHM with increasing grid size. The RMSE of T-MHM is relatively flat in the East and North directions. The RMSE of the T-MHM with a grid size of 1×1 is equivalent to that of MHM grid size divided into 9×9 in these two directions. In the vertical direction, the RMSE tends to increase linearly, and the results of RMSE with T-MHM grid size divided into 9×9 and those of the MHM with grid size 2×2 are similar.

We also investigate the convergence time of MHM and T-MHM for the nine different grid sizes. The statistics of the three directions are illustrated in Fig. 14. It can be seen that the convergence time of T-MHM tends to be more stable as the grid size increases. The convergence time of T-MHM is about 3–5 times shorter than that of MHM. Especially in the vertical direction, the maximum increase of T-MHM is about 90% (from 88.6 to 9.2 min) for the same grid size.

Fig. 8 STD (m) of positioning errors in East, North, and Vertical directions using modeling from days 4–7 (DOY 275–278)
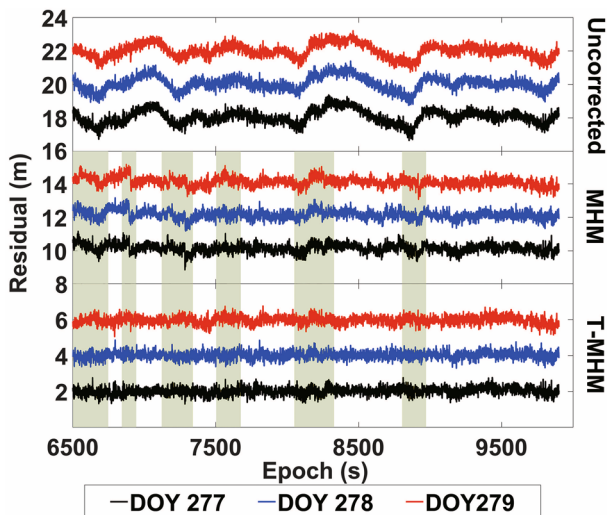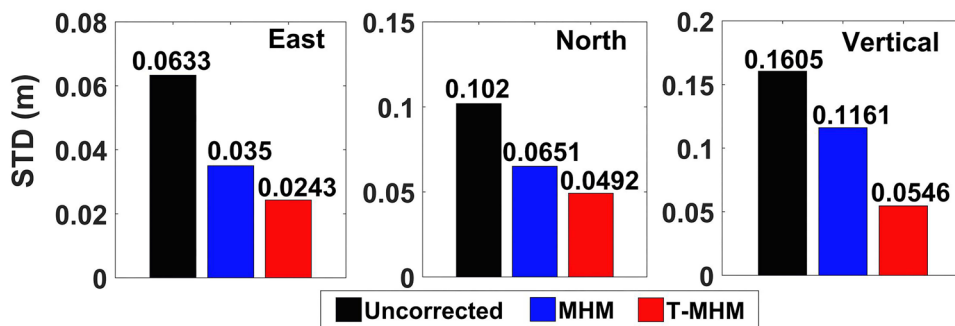

Table 3 STD (m) of each residual sequence in Fig. 9

		Pseudorange		Carrier phase	
DOY 277	Uncorrected	0.4117	Correction rate	0.0050	Correction rate
	MHM	0.2610	36.6%↑	0.0030	40.0%↑
	T-MHM	0.2172	47.3%↑	0.0024	52.0%↑
DOY 278	Uncorrected	0.4127	Correction rate	0.0057	Correction rate
	MHM	0.2656	35.6%↑	0.0034	40.4%↑
	T-MHM	0.2099	49.1%↑	0.0024	57.9%↑
DOY 279	Uncorrected	0.4086	Correction rate	0.0051	Correction rate
	MHM	0.2770	32.2%↑	0.0033	35.3%↑
	T-MHM	0.2269	44.5%↑	0.0024	53.0%↑
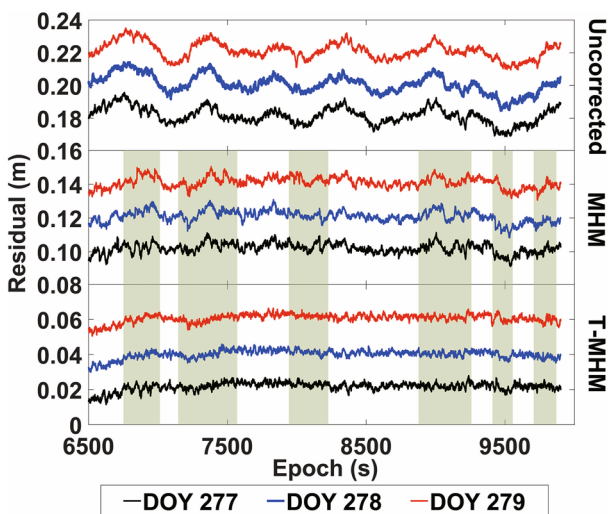
Fig. 9 PRN 02 pseudorange (top) and carrier phase (bottom) residuals for epochs 6500–10,000 (DOY 277279) for the multipath uncorrected case and the model correction cases MHM and T-MHM

Therefore, the T-MHM has high robustness to the sky grid size division, which can appropriately increase the sky grid size and improve operation efficiency.

Conclusions and remarks

The multipath, which is considered the main unmodeled error source, limits the GPS high-precision positioning at centimeter level or better in a complex urban environment. Previous studies had indicated that the multipath mitigation method based on spatial repeatability could effectively correct the multipath error. The T-MHM trend-surface analysis method can fit the spatial distribution of multipath inside the grid and effectively alleviate the high-frequency multipath error, which a normal MHM could not correct. At present, the T-MHM method has proven ideal only for the differential mode (Wang et al. 2019, 2020). We demonstrated the applications of T-MHM in PPP mode and analyzed its performance. The conclusions are as follows:

Based on our experiments, the optimal observation span for the T-MHM modeling is 4–7 days. Compared to the original MHM model, the T-MHM can significantly improve the positioning accuracy and convergence time. The positioning accuracy in the horizontal and vertical directions can be improved by 21.6 and 13.6%, and the convergence time can be shortened by 24.2 and 7.2%, respectively.

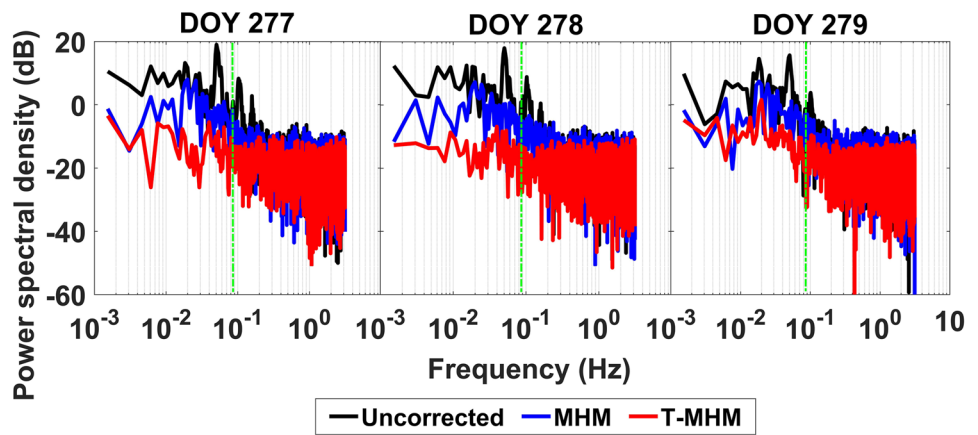**Fig. 10** Power spectral density of carrier phase residual sequence of Fig. 9

Table 4 Features of Allan deviation plots for typical noise terms (Niu et al. 2014)

Noise type	Curve slope	Characterization parameters	Detailed notes
White noise (WN)	− 1/2	$Q = \sigma(1)$	Q—the WN noise intensity
Random walk noise	+ 1/2	–	T_{max}—the GM cluster time, σ_{GM}—the G
Gaussian Markov noise (GM)	± 1/2	$T_c = \frac{T_{max}}{1.89}, Q_c = \frac{2\sigma_{GM}^2}{T_c}$	Allan deviation, Q_c—the GM noise intensity
Flicker noise	0	–	

Fig. 11 Allan deviation plots for PRN 02 pseudorange (top) and carrier phases (bottom) between epochs 6500 and 10,000 as a function of cluster time. The purple and green marks indicate the positions of WN and GM parameters, respectively
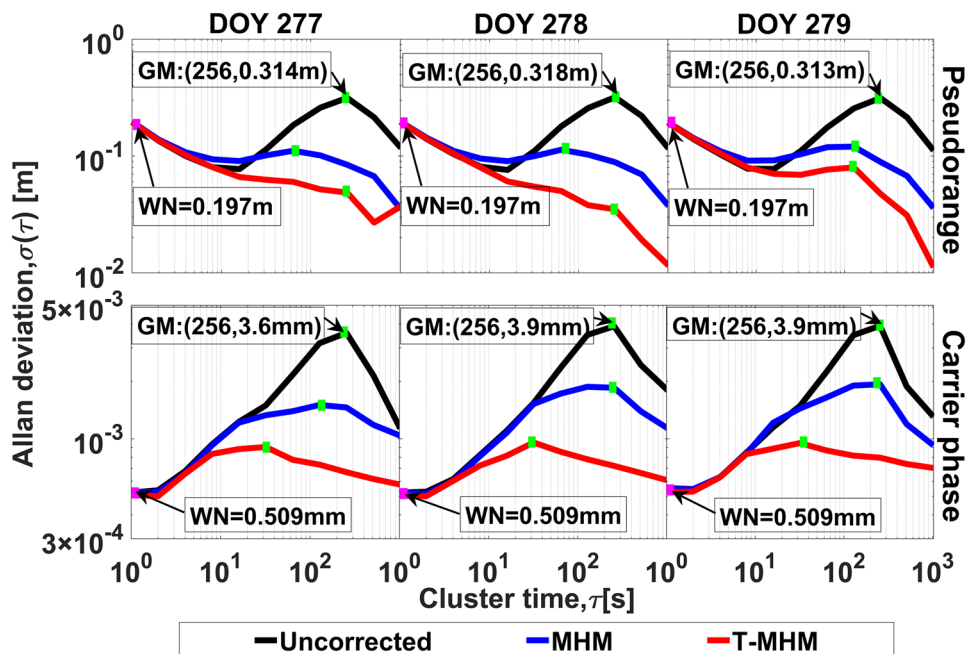
We extracted 3 days of residuals from the optimal modeling results. The power spectral density analysis shows that T-MHM can effectively correct the high- and low-frequency multipath, and the corrected residual sequence is close to WN. In time-domain Allan variance analysis, the noise combination can be determined as WN and GW, while the T-MHM can significantly reduce the noise intensity of the GM and ensure that the frequency of the residual sequence is stable.

We discuss the impact of MHM and T-MHM modeling on the correction results under different grid sizes. The T-MHM yields higher positioning accuracy and a more
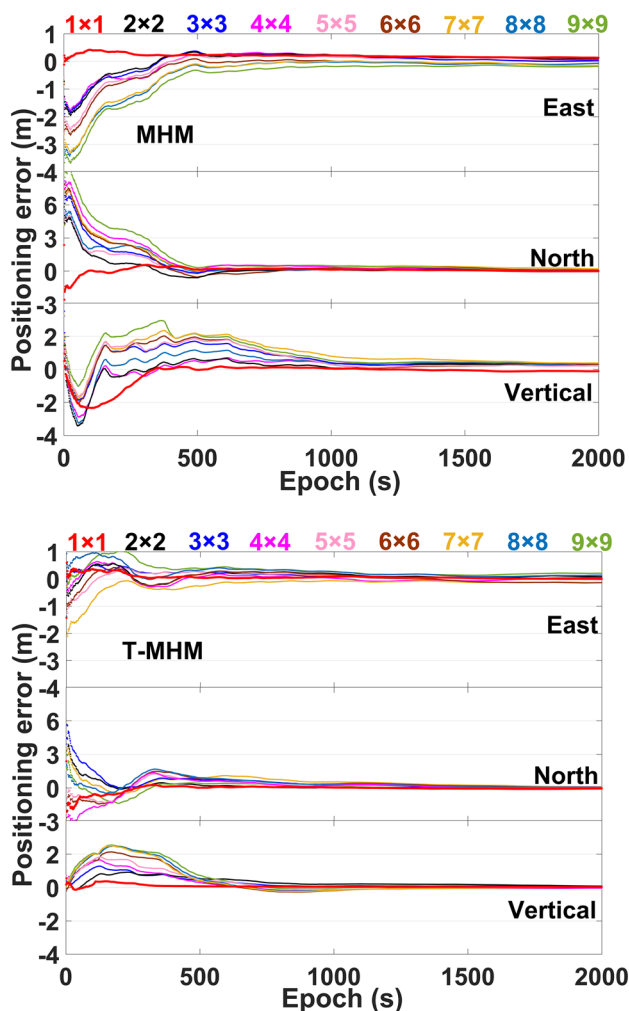
Fig. 12 Comparison of positioning errors with different grid sizes for MHM (top) and T-MHM (bottom). On the top of each panel, the n × m indicates the size of the grid with n being the azimuth interval *m*. the elevation angle interval
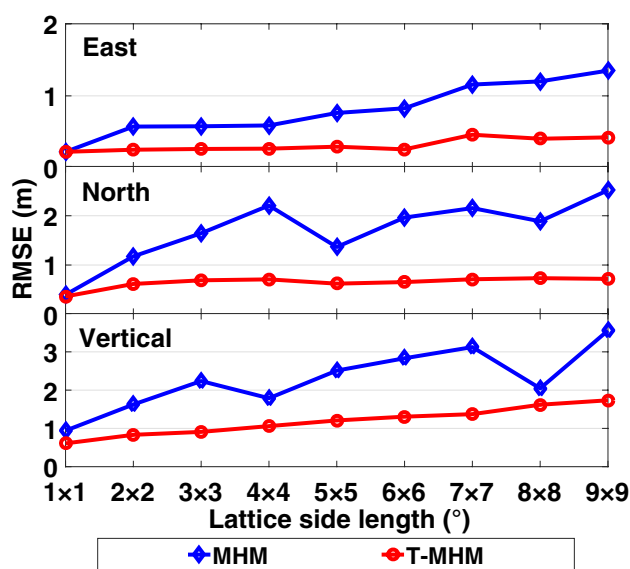

Fig. 13 RMSE of MHM and T-MHM with different grid sizes
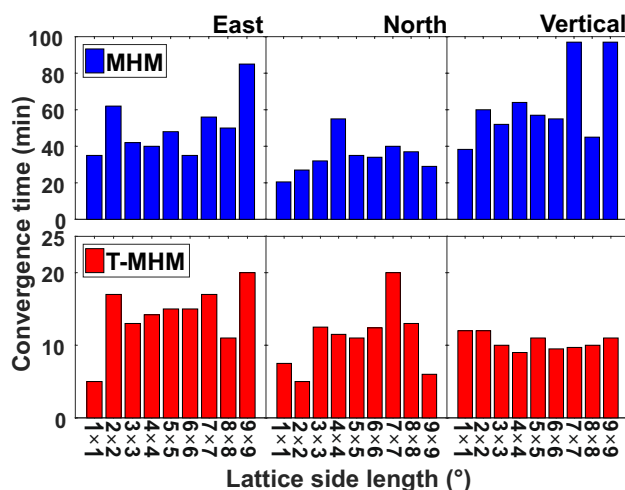

Fig. 14 Convergence time for different grid sizes. Top and bottom panels refer the MHM and T-MHM, respectively

stable convergence time than MHM, with increasing grid size. Therefore, T-MHM has high robustness for solving PPP, because one can efficiently increase the grid size of T-MHM and promote computational efficiency.

The excellent performance of T-MHM in PPP mode is achieved due to the following reasons:

In a high obstruction urban environment, the multipath interference and NLOS error coexist, and they are generated through different mechanisms. The mean value of the residuals inside the grid is used in the ordinary multipath hemispherical map. As a result, the spatial variation of the residuals inside the grid is overlooked. The T-MHM performs a trend-surface fitting on the spatial variation of the

residuals inside the grid, which eliminates possible over-correction and an insufficient correction.

The proportion of high-frequency multipath in the urban environment is larger than in the open environment due to the many obstructions. One of the most important advantages of T-MHM is that it can correct the high-frequency structure inside the grid, thus making it suitable for use in high-density urban environments

A small positioning error persists during the convergence process even after T-MHM corrects the multipath error. Such a phenomenon could be attributable because the anti-jamming

ability of pseudorange is much weaker than that of the carrier phase, which leads to a stronger spatial variability of pseudorange multipath error inside grid points. Therefore, T-MHM has some limitations in pseudorange multipath error correction and requires further analysis.

At present, the research on T-MHM is limited to GPS systems. In urban environment, multi-GNSS can provide more visible satellites and uniform spatial coverage. Unlike GPS only, the cycle repeatability of each GNSS system differs. Therefore, we discuss the actual modeling conditions according to the repetition characteristics of different systems and constellations in future work. Also, the high-frequency multipath is very apparent in ships and aircraft platforms. Thus, the correction benefits of T-MHM in such dynamic environments are also subject of further investigation.

Data Availability The data used in this manuscript are available from the corresponding author upon request.

References

Atkins C, Ziebart M (2016) Effectiveness of observation-domain sidereal filtering for GPS precise point positioning. GPS Solut 20(1):111–122. https://doi.org/10.1007/s10291-015-0473-1

Banville S, Tang H (2010) Antenna rotation and its effects on kinematic Precise point positioning. In: Proceedings ION GNSS 2010, Institute of Navigation, Portland, OR, September 21–24, pp 2545–2552

Bock Y, Nikolaidis RM, Jonge PJ, Bevis M (2000) Instantaneous geodetic positioning at medium distances with the Global Positioning System. J Geophys Res Solid Earth 105(B12):28223–28253

Choi K, Bilich A, Larson KM, Axelrad P (2004) Modified sidereal filtering: implications for high-rate GPS positioning. Geophys Res Lett. https://doi.org/10.1029/2004gl021621

Cohen CE, Parkinson BW (1991) Mitigating multipath error in GPS based attitude determination. Adv Astronaut Sci 74:53–68

Collins P (2008) Isolating and estimating Undifferenced GPS integer ambiguities. In: Proceedings ION NTM 2008, Institute of Navigation, San Diego, CA, January 28–30, pp 720–732

Dai W, Ding X, Zhu JJ, Chen YQ, Li ZW (2006) EMD Filter Method and Its Application in GPS Multipath. Acta Geodaetica Et Cartographica Sinica 35(4):321–327

Dierendonck AJV, Fenton P, Ford T (1992) Theory and performance of narrow correlator spacing in a GPS receiver. J Inst Navig 39(3):265–283. https://doi.org/10.1002/j.2161-4296.1992.tb022 76.x

Dinius AM (1995) GPS antenna multipath rejection performance. Nasa Sti/Recon Tech Rep N 96(58):16–21. https://doi.org/10.1002/wilm.10088

Dong D, Wang M, Chen W, Zeng Z, Song L, Zhang Q, Cai M, Cheng Y, Lv J (2016a) Mitigation of multipath effect in GNSS short

baseline positioning by the multipath hemispherical map. J Geod 90(3):255–262. https://doi.org/10.1007/s00190-015-0870-9

Dong D, Chen W, Cai M, Zhou F, Wang M, Yu C, Zheng Z, Wang Y (2016b) Multi-antenna synchronized global navigation satellite system receiver and its advantages in high precision positioning applications. Front Earth Sci 10(4):772–783

Fuhrmann T, Luo X, Knöpfer A, Mayer M (2015) Generating statistically robust multipath stacking maps using congruent cells. GPS Solut 19(1):83–92. https://doi.org/10.1007/s10291-014-0367-7

Ge L, Rizos C, Han S, Sc B, Sc M (2000) Multipath mitigation of continuous GPS measurements using an adaptive filter. GPS Solut 4(2):19–30. https://doi.org/10.1007/PL00012838

Geng J, Bock Y (2016) GLONASS fractional-cycle bias estimation across inhomogeneous receivers for PPP ambiguity resolution. J Geod 90(4):379–396. https://doi.org/10.1007/s00190-015-0879-0

Genrich JF, Bock Y (1992) Rapid resolution of crustal motion at short ranges with the Global Positioning System. J Geophys Res Solid Earth 97(B3):3261–3269

Gill M, Bisnath S, Aggrey J, Seepersad G (2017) Precise point positioning (PPP) using low-cost and ultra-low-cost GNSS teceivers. In: Proceedings ION GNSS 2017, Institute of Navigation, Portland, Oregon, September 25–29, pp 226–236

Groves PD, Jiang Z (2013) Height aiding, C/N0 weighting and consistency checking for GNSS NLOS and multipath mitigation in urban areas. J Navig 66:653–669. https://doi.org/10.1017/S0373 463313000350

Groves PD, Jiang Z Skelton B, Cross PA (2010) Novel multipath mitigation methods using a dual-polarization antenna. In: Proceedings ION GNSS 2010, Institute of Navigation, Portland, Oregon, September 2010 21–24, pp 140–151

Hung HK, Rau RJ (2013) Surface waves of the 2011 Tohoku earthquake: observations of Taiwan's dense high-rate GPS network. J Geophys Res Solid Earth 118:332–345. https://doi.org/10.1029/2012JB009689

IEEE (2008a) Standard specification format guide and test procedure for linear single-axis, non-gyroscopic accelerometers. IEEE Std 1293–1988:166–182

IEEE (2008b) Standard specification format guide and test procedure for single-axis interferometric fiber optic gyros. IEEE Std 952–1997(R2008):61–73

Kouba J (2015) A guide to using international GNSS service (IGS) products. https://kb.igs.org/hc/en-us/articles/201271873-A-Guide-to-Using-the-IGS-Products. Accessed 15 Sept 2019

Li P, Zhang X (2014) Integrating GPS and GLONASS to accelerate convergence and initialization times of precise point positioning. GPS Solut 18(3):461–471. https://doi.org/10.1007/s10291-013-0345-5

Li B, Zhang Z, Shen Y, Yang L (2018) A procedure for the significance testing of unmodeled errors in GNSS observations. J Geod 92:1171–1186

Liu T, Yuan Y, Zhang B, Wang N, Chen Y (2017) Multi-GNSS precise point positioning (MGPPP) using raw observations. J Geod 91(3):253–268. https://doi.org/10.1007/s00190-016-0960-3

Malys S, Jensen PA (1990) Geodetic point positioning with GPS carrier beat phase data from the CASA UNO experiment. Geophys Res Lett 17(5):651–654

Nee RDJV (1995) Multipath and multi-transmitter interference in spread-spectrum communication and navigation systems. Dissertation, Delft University

Nee RDJV, Siereveld J, Fenton PC, Townsend BR (1994) The multipath estimating delay lock loop: approaching theoretical accuracy limits. In: Proceedings of 1994 IEEE position, location and navigation symposium–PLANS'94, Las Vegas, NV, USA, pp 246–251 https://doi.org/10.1109/PLANS.1994.303320

Niu X, Chen Q, Zhang Q, Niu J, Chen K, Shi C, Liu J (2014) Using Allan variance to analyze the error characteristics of GNSS positioning. GPS Solut 18:231–242. https://doi.org/10.1007/s10291-013-0324-x

Pan L, Zhang X, Liu J (2019) A comparison of three widely used GPS triple-frequency precise point positioning models. GPS Solut. https://doi.org/10.1007/s10291-019-0914-3

Ragheb AE, Clarke PJ, Edwards SJ (2007) GPS sidereal filtering: coordinate- and carrier-phase-level strategies. J Geod 81(5):325–335

Riley WJ (2008) Handbook of frequency stability analysis, US Department of Commerce, National Institute of Standards and Technology

Su M, Zheng J, Yang Y, Wu Q (2018) A new multipath mitigation method based on adaptive thresholding wavelet denoising and double reference shift strategy. GPS Solut 22(2):40. https://doi.org/10.1007/s10291-018-0708-z

Takasu T (2006) High-rate precise point positioning: observation of crustal deformation by using 1-Hz GPS data. In: GPS/GNSS Symposium, Tokyo

Wang Z, Chen W, Dong D, Wang M, Cai M, Yu C, Zheng Z, Liu M (2019) Multipath mitigation based on trend surface analysis applied to dual-antenna receiver with common clock. GPS Solut. https://doi.org/10.1007/s10291-019-0897-0

Wang Z, Chen W, Dong D, Zhang C, Peng Y, Zheng Z (2020) An advanced multipath mitigation method based on trend surface analysis. Remote Sens 12:3601

Wu JT, Wu SC, Hajj G, Bertiger WI, Lichten SM (1993) Effects of antenna orientation on GPS carrier phase. Manuscr Geod 18(2):91–98

Zhang X, Zuo X, Pan L (2013) Mathematic model and performance comparison between Ionospherefree combined and uncombined precise point positioning. Geomat Inf Sci Wuhan Univ 38(5):561–565

Zhang X, Zhu F, Xue X, Tang L (2015) Using Allan Variance to Analyze the Zero-differenced Stochastic Model Characteristics of GPS. Acta Geod Cartogr Sinica 44(2):119–127s

Zhao J, Hernández-Pajares M, Li Z, Wang L, Yuan H (2020) High-rate Doppler-aided cycle slip detection and repair method for low-cost single-frequency receivers. GPS Solut. https://doi.org/10.1007/s10291-020-00993-0

Zheng K, Zhang X, Li P, Li X, Ge M (2019) Multipath extraction and mitigation for high-rate multi-GNSS precise point positioning. J Geod 93(10):2037–2051

Zhong P, Ding X, Zheng D, Chen W, Huang D (2008) Adaptive wavelet transform based on cross-validation method and its application to GPS multipath mitigation. GPS Solut 12(2):109–117. https://doi.org/10.1007/s10291-007-0071-y

Zhong P, Ding X, Yuan L, Xu Y, Kwok KCS, Chen Y (2010) Sidereal filtering based on single differences for mitigating GPS multipath effects on short baselines. J Geod 84(2):145–158. https://doi.org/10.1007/s00190-009-0352-z

Zhou F (2020) Theory and methodology of multi-GNSS undifferenced and uncombined precise point positioning. Acta Geod Cartogr Sinica 49(7):938

Zhou F, Dong D, Li W, Jiang X, Wickert J, Schuh H (2018) GAMP: an open source software of multi-GNSS precise point positioning using undifferenced and uncombined observations. GPS Solut. https://doi.org/10.1007/s10291-018-0699-9

Zimmermann F, Eling C, Kuhlmann H (2017) Empirical assessment of obstruction adaptive elevation masks to mitigate site-dependent effects. GPS Solut 21(1):1–12

Zumberge J, Heflin M, Jefferson D, Watkins M, Webb F (1997) Precise point positioning for the efficient and robust analysis of GPS data from large networks. J Geophys Res 102(B3):5005–5017. https://doi.org/10.1029/96JB03860

Ran Lu is currently a M.S. candidate at East China Normal University, Shanghai, China. He recently focused on applying GNSS precise point positioning in an urban environment and processing unmodeled errors.

Wen Chen received her PhD degree in geospatial information science (GIS) from East China Normal University in 2010. She currently works as an associate professor of the School of Geographic Sciences at East China Normal University. Her major research interests include GNSS high-precision positing and applications, spatial analysis, and GIS.


Danan Dong is currently a professor at East China Normal University. He obtained his PhD degree from the Massachusetts Institute of Technology (MIT) and had worked in Jet Propulsion Laboratory (JPL) for 18 years. His main research interest is in the study of GNSS positioning and geophysics with the application of GPS technology.

Zhiren Wang received her PhD degree in East China Normal University, Shanghai, China. Her interests include GNSS data processing and multipath mitigation algorithm. She recently focused on developing algorithms to detect and model NLOS, which can be applied to lane-level vehicle and high-precision pedestrian locationing in high-density urban areas.

Yu Peng received her PhD degree in geophysics at East China Normal University in 2019. She currently works as a postdoctor at the School of Geographic Sciences, East China Normal University. Her major research interests focus on GNSS high-precision positioning and applications.
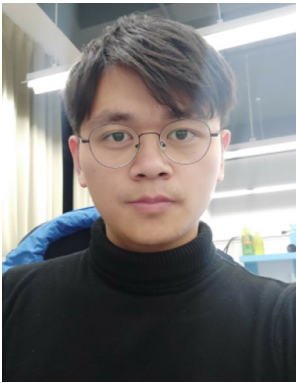
Chenglong Zhang is currently a PhD candidate in East China Normal University, Shanghai, China. His interests include single difference ambiguity fixed and attitude position by multi-antenna synchronized GNSS receiver.

Chao Yu received his PhD degree in physical electronics from the Shanghai Institute of Technical Physics of Chinese Academy of Sciences in 2005. He currently works as a senior engineer of the School of Information Science Technology at East China Normal University. His major research interests include GNSS information processing and application.